Upconversion and Optical Nanothermometry in $LaGdO_3$: Er^{3+} Nanocrystals in the RT-900 K Range

Journal:	*The Journal of Physical Chemistry*
Manuscript ID	jp-2019-06959u.R1
Manuscript Type:	Article
Date Submitted by the Author:	03-Oct-2019
Complete List of Authors:	Gutierrez Cano, Vanessa; Universidad de Cantabria, DCITIMAC Rodríguez, Fernando ; Universidad de Cantabria González, Jesús; Universidad de Cantabria Valiente, Rafael; Universidad de Cantabria

Upconversion and Optical Nanothermometry in $LaGdO_3$: Er^{3+} Nanocrystals in the RT-900 K Range

Vanessa Gutiérrez-Cano,*,† Fernando Rodríguez,† Jesús A. González,† and Rafael Valiente‡

†*DCITIMAC, Facultad de Ciencias, Universidad de Cantabria, 39005 Santander, Spain*

‡*Dpto. Física Aplicada, Facultad de Ciencias, Universidad de Cantabria–IDIVAL, 39005 Santander, Spain.*

E-mail: vanesa.gutierrezcano@unican.es

Abstract

The search of material hosts being able to incorporate Er^{3+} impurities with a thermally stable structure and high melting temperature is priority in optical thermometry. In this work, we report on the structural and spectroscopic characterization of Er^{3+}–doped and Yb^{3+}/Er^{3+}–co-doped $LaGdO_3$ nanocrystals synthesized via the sol-gel Pechini method. X-ray diffraction and Raman spectroscopy unequivocally show that the synthesis method provides nanocrystals with a single-phase *B*-type monoclinic structure (space group: *C2/m*). Intensity decay curves *I(t)* were measured to investigate the efficiency of upconversion processes yielding green emission. We showed that an energy transfer upconversion (ETU) process involving Yb–Er pairs governs visible emission upon NIR excitation. The temperature dependence of the thermalized green luminescence at 525 nm ($^2H_{11/2}\rightarrow{}^4I_{15/2}$) and 549 nm ($^4S_{3/2}\rightarrow{}^4I_{15/2}$) was checked for thermometric applications in the RT–900 K temperature range. We demonstrate that the *B*-type monoclinic phase of $LaGdO_3$ is stable from low temperature up to 900 K. Doped with Er^{3+}, it shows suitable thermometer capabilities with a maximum sensitivity of $S = 4.3{\cdot}10^{-3}$ K^{-1} at 554 K, and a relative sensitivity decreasing from its maximum value at 0 K to $S_R = 1.2 \cdot 10^{-2}$ K^{-1} at 298 K. The results suggest that $LaGdO_3$ in its *B*-type monoclinic phase is a promising material as a wide-range temperature sensor, without any further surface protection.

Introduction

Lanthanide doped nanophosphors have drawn much attention in the last years regarding their luminescence properties as they cover a wide range of applications such as solid-state lasers, LEDs, bio-imaging, photothermal therapy, nanothermometry, IR viewers, etc.[1–8] Fluorescence thermometry is based on the fluorescence intensity ratio (*FIR*) technique arising from two thermalized emitting levels characteristic of certain rare-earth ions like Er^{3+}.[9] At variance with thermometers based on transition-metal-ions like Cr^{3+} (ruby), those using rare-earth-based *FIR* are more suitable for thermometry since energy levels are weakly

dependent on the crystal field and its applicability can be guaranteed in different host materials. The energy levels of transition-metal ions are, in general, strongly dependent on the crystal field and luminescence can easily quench by increasing temperature, both effects limiting their application as optical thermometers only to few materials.[10] The most widely used ion for optical thermometry is Er^{3+}, which $^4S_{3/2}$ and $^2H_{11/2}$ thermally coupled levels provide high luminescence efficiency, good spectral resolution and sensitivity for temperature measurements.[11] Furthermore, its temperature sensitivity can be improved via infrared (IR) upconversion (UC) excitation of Er^{3+} since it reduces significantly the luminescence background -autofluorescence- of biological systems with respect to a direct excitation process.[12] In addition, it is important in bio-thermometry due to the suitability of IR radiation to penetrate in biological tissues and minimize radiation damage.[13] Moreover, the use of nanostructured hosts broadens the applicability of these materials as they can be incorporated to other non-optically active materials or biological systems via core-shell functionalization,[14] and thus providing them with an *in-situ* thermometer (temperature control), nanophosphor (imaging) or local heater (hyperthermia).

Recently, Siaï *et al.*[15] have proposed $LaGdO_3$ as a promising host material for optical thermometry due to its low-phonon energy, optical inactivity of La^{3+}, and UV emission of Gd^{3+}. Its structural similarity to $NaYF_4$ foresees this material as an efficient UC host material provided that it can be stabilised in the monoclinic *C2/m* phase.[16–18] $LaGdO_3$ is advantage with respect to other host materials because of its higher melting temperature (above 1400 K) and better capability for integration in oxides/glasses. Additionally, it shows a good lattice mismatch with silicon, what is interesting for electronic thermometry applications.[17]

The important role played by the crystal structure in the UC efficiency has been shown in $NaYF_4$.[18] The UC luminescent efficiency of green emission in β-$NaYF_4$: Er^{3+}/Yb^{3+} phase is about 10 times higher than in α-$NaYF_4$: Er^{3+}/Yb^{3+}.[18,19] Furthermore, the concentration of optically active doping agents is also directly related to its luminescence efficiency due to

two opposite effects: increasing the Yb-Er-Yb coupled systems favoring UC processes, and the energy transfer among Er^{3+} ions yielding green upconversion luminescence quenching[20] by cross-relaxation. In Er^{3+}/Yb^{3+} co-doped systems, investigations devoted to establish the optimum concentrations of each dopant is crucial to get the best UC efficiencies hence maximum temperature sensitivity. Optimum doping concentrations of 2% Er^{3+} and 20% Yb^{3+} were found for hexagonal $NaYF_4$ in both α and β phases.[18]

$LaGdO_3$ belongs to the family of perovskite-type ABO_3 compounds, with a big trivalent cation, A, and a small trivalent cation, B. The former having seven neighboring oxygens that are coordinated with A ions along x-axes and B ions along y-axes (Fig. 1). Namely, $LaGdO_3$ has a B-type monoclinic *C2/m* structure (a=14.43 Å, b=3.69 Å, c=9.00 Å; β=100.70°) at ambient conditions.[16,17]

Typically, *RE-RE'*O_3 (*RE* and *RE'* = rare earth elements) binary mixed pervoskite oxides usually crystallize in three different structures: hexagonal, monoclinic or cubic. The crystal structure of the formed compound depends on the crystal structure of the starting compounds RE_2O_3 and RE'_2O_3, as well as on the adequacy of the Goldschmidt tolerance factor:[21,22]

$$t = \frac{(r_A + r_O)}{\sqrt{2}(r_B + r_O)} \quad (1)$$

where r_A is the radius of the A-cation, r_B of the B-cation and r_O of the anion (in this case oxygen). t values close to 1 corresponds to cubic perovskite structures, whereas smaller t values give rise to distorted perovskites, the orthorhombic structure being the most common one. In La*RE*O_3, the radius difference between La^{3+} and other *RE* ions provides t values far from 1, and all compounds show an orthorhombic structure with the exception of the monoclinic $LaDyO_3$.[23] The use of high-pressure and high-temperature synthesis conditions favors stabilization of monoclinic phases in perovskite oxides.[16,24,25]

In this work, we report on the synthesis of $LaGdO_3$ in a monoclinic single phase *via*

a modified sol-gel method, and its structural characterization by means of X-ray diffraction (XRD) and Raman spectroscopy. Additionally, we investigate the effect of Er^{3+} and Er^{3+}/Yb^{3+} doping on the crystal structure and their Er^{3+} photoluminescence (PL) properties, in particular, those related to the optimum doping concentration for temperature sensing. UC mechanisms are also investigated through time-resolved spectroscopy.

Experimental section

Synthesis

$LaGdO_3$: x% Er^{3+} (x = 0.1, 1, 2, 5) and 2% Er^{3+}, 20% Yb^{3+} nanocrystals were synthesized by a slightly modified sol-gel Pechini method using $La(NO_3)_3{\cdot}6H_2O$ (99.9%), $Gd(NO_3)_3{\cdot}6H_2O$ (99.9%), $Er(NO_3)_3{\cdot}6H_2O$ (99.9%), $Yb(NO_3)_3{\cdot}6H_2O$ (99.9%), citric acid (99%), from Alfa Aesar, and polyethylene glycol 10000 (PEG), from Merck, as starting materials. Stoichiometric amounts of nitrates were dissolved in distilled water together with citric acid in a 2:1 citrate:nitrate molar ratio and the solution was heated up at 90 ºC under stirring. Then, PEG was added to the solution and it was stirred for additional 15 min. Finally, the obtained sol was heated up at 90 ºC for 24 h to form the amorphous gel that was then calcined at 1200 ºC for 8h.

Characterization techniques

Powder XRD was performed using a Bruker D8 Advance diffractometer in the range 5º-80º, Cu-K_α radiation, a scan step of 0.02º and scan speed of 0.5 º/min.

Raman spectra were acquired in backscattering configuration with a Horiba T64000 Raman spectrometer equipped with a triple monochromator in the substractive configuration (spectral resolution of 0.6 cm^{-1}) coupled to a confocal microscope. The 488 and 647 nm lines of a coherent Innova Spectrum 70C Ar^+-Kr^+ laser were used as excitation sources, and a liquid-nitrogen-cooled CCD (Jobin-Yvon Symphony) was used as low-noise detector. Tem-

perature dependent measurements in the 298-873 K range were performed with a heating stage Linkam TS1000 coupled to the T64000 spectrometer, using a 20× objective and a laser power output of 1 mW on sample. The intensity-to-temperature calibration procedure was performed by placing the nanocrystals in thermal contact with the temperature controller during 5 min for each temperature step before collecting the emission spectrum.[26]

Absorption spectra were acquired in a CARY 6000i spectrophotometer (Varian) in the 200–1700 nm range with an integrating sphere. Luminescence spectra and decay curves were obtained by exciting the samples with a 980 nm DPSSL externally modulated laser (Shanghai Laser & Optics Century 160 Co., Ltd) and emissions were analyzed with a spectrofluorimeter FLSP920 from Edinburgh Instruments using multichannel scaling (MCS) technique.

Results and discussion

XRD structural characterization

Structural studies of both Er^{3+}-doped, Er^{3+}/Yb^{3+}-co-doped and undoped-$LaGdO_3$ powders are shown in Fig. 2. All XRD patterns were successfully fitted to a B-type monoclinic crystal structure (space group $C2/m$) using the FullProf Suite software.[27] Lattice parameters obtained after Rietveld structure refinement, together with the fitting goodness, are collected in Table 1. The fitting quality confirms formation of single-phase nanocrystals in all investigated samples. Besides the B-type monoclinic structure, no evidences of secondary phases or impurities are detected from powder XRD, within the experimental uncertainty. The structure (Fig. 1) consists of 7-fold coordinated polyhedra, which are linked to each other through oxygen-edge sharing. The reported distances between La-O and Gd-O are in the 2.1-2.9 Å range, with an average value of 2.6 ± 0.3 Å in both cases. Furthermore, the average distances between metal ions are: La-La 3.8 ± 0.1 Å, Gd-Gd 3.7 ± 0.1 Å and La-Gd 3.8 ± 0.3 Å. Therefore, this structure provides equivalent *RE*-substitutional and different interstitial sites for dopant replacement, thus favoring multisite formation.[17]

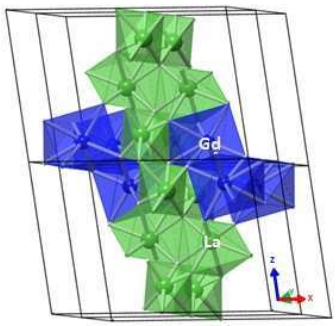

Figure 1: Representation of the $LaGdO_3$ unit cell highlighting the La (green) and Gd (blue) 7-fold coordination environments.

Figure 2(a) shows the Rietveld refined XRD pattern of undoped $LaGdO_3$ at room temperature. The simulated profile shows a fairly good agreement with the measured pattern. The obtained unit cell parameters, $a = 14.448$ Å, $b = 3.694$ Å, $c = 9.010$ Å, $\beta = 100.7°$, agree with those reported elsewhere.[16,17] By doping with Er^{3+}, and doubly doping with Er^{3+}/Yb^{3+} (Figs. 2 (b-c)), we obtain the same crystal structure –uncollapsed structure– resulting in a lattice-cell shortening –chemical compression– (see Table 1). This effect is explained by the lanthanide contraction, where the addition of electrons to the shielded *4f* orbitals results in an increase of the effective nuclear charge yielding decrease of ionic radii.[28,29] This lattice reduction with doping is due to replacement of Gd^{3+} and La^{3+} ions by the dopant ions, the ionic radii of which are smaller than the host ions (Gd^{3+}: r = 1.00 Å; La^{3+}: r = 1.16 Å; Er^{3+}: r = 0.945 Å; Yb^{3+}: r=0.925 Å).[30]

Table 1: Lattice parameters and unit cell volume as a function of the nominal concentration of doped and undoped $LaGdO_3$ samples.

Sample	a (Å)	b (Å)	c (Å)	β (º)	V (Å^3)	R_B(%)
$LaGdO_3$	14.448(1)	3.694(1)	9.010(1)	100.7(1)	472.5(4)	9.1
$LaGdO_3$: 0.1% Er^{3+}	14.443(2)	3.696(1)	9.012(6)	100.7(1)	472.7(7)	4.6
$LaGdO_3$: 1% Er^{3+}	14.459(2)	3.699(1)	9.021(1)	100.8(1)	474.0(4)	5.2
$LaGdO_3$: 2% Er^{3+}	14.432(1)	3.687(1)	8.998(1)	100.7(1)	470.5(3)	3.9
$LaGdO_3$: 5% Er^{3+}	14.412(1)	3.678(1)	8.981(1)	100.8(1)	467.7(3)	3.6
$LaGdO_3$: 2% Er^{3+}, 20%Yb^{3+}	14.375(1)	3.646(1)	8.933(1)	101.0(1)	459.6(5)	9.7

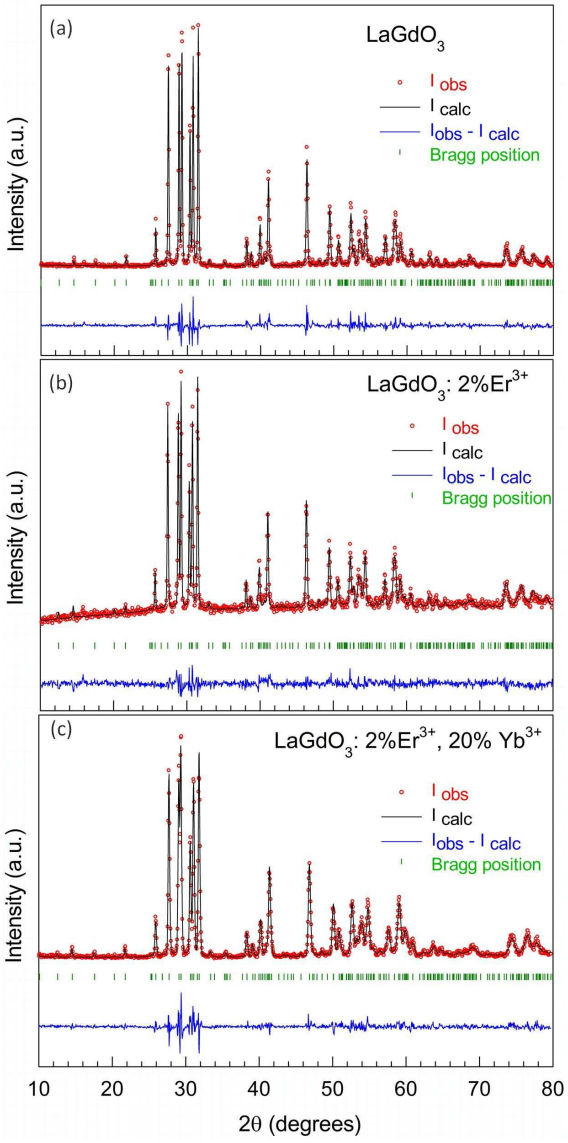

Figure 2: Measured and calculated x-ray diffraction patterns (in red and black, respectively) together with Bragg peak positions (in green) after final Rietveld refinement of pure $LaGdO_3$ (a), $LaGdO_3$: 2% Er^{3+} (b) and $LaGdO_3$: 2% Er^{3+}, 20% Yb^{3+} (c).

Raman spectroscopy

Pure $LaGdO_3$ was also analyzed by Raman spectroscopy at ambient pressure. Group theory for the monoclinic structure (space group $C/2m$) allows 42 optical vibrational modes at Γ_o point:[31] 14A_g (R) + 7 B_g (R) + 7A_u (IR) + 14 B_u (IR), where 21 are Raman active (R) and 18 are infrared active (IR). The room temperature (RT) Raman spectrum of pure $LaGdO_3$ shows 13 out of the 21 active modes (Fig. 3). At low temperatures (90 and 4 K)

additional modes can be observed, like the A_g mode at 256 cm^{-1} and the B_g modes at 301 and 432 cm^{-1}. Table 2 collects the frequency of the observed vibration modes at 4, 90 and 300 K (RT), together with a tentative mode assignment following Raman results reported elsewhere.[17,32]

The main features observed in the Raman spectra at different temperatures are the following: (i) the low-frequency modes below 270 cm^{-1} are almost temperature independent (softening between 2-3 cm^{-1}), with the exception of the 167 cm^{-1} phonon, which experiences a hardening of 12 cm^{-1} upon heating from 4 K to 300 K; (ii) modes with frequencies between 350-475 cm^{-1} at RT are more intense than the low-temperature ones in comparison to the low-frequency phonon behavior; (iii) by contrast, broad bands between 500-800 cm^{-1} are broader and more intense at low temperatures (4 K); (iv) most of the mid frequency modes (200 - 450 cm^{-1}) are better resolved at low temperatures; (v) four peaks are resolved at low temperature, three of them being identified as A_g and B_g modes; (vi) the two broad bands located around 556 and 681 cm^{-1} (671 and 677 nm, respectively) do correspond to luminescence peaks from unintentional Er^{3+} impurities.[32] Actually, their intensity increases with respect to the Raman peak intensities with increasing Er^{3+} concentratio in $LaGdO_3$: Er^{3+}. In addition, these broad bands do not appear in the Raman spectrum taken under laser excitation at 488 nm, where two new Raman peaks –masked in the 647 nm Raman spectrum– are now visible at 531 and 637 cm^{-1}. It must be emphasized that an adequate and complete phonon assignment on the basis of the monoclinic $C2/m$ phase cannot be properly achieved due to peak broadening and overlap, making the mode analysis hard to accomplish.

Electronic absorption and photoluminescence at ambient conditions

The absorption spectrum of $LaGdO_3$: 2% Er^{3+}, 20% Yb^{3+} in the UV-VIS-NIR region is shown in Fig. 4. The characteristic absorption peaks of Er^{3+} can be identified to *f-f* intra-configurational electronic transitions from the $^4I_{15}/_2$ ground state to different excited states: $^4I_{15}/_2 \rightarrow ^4G_{11}/_2$ (379 nm), $^2H_9/_2$ (408 nm), $^2F_3/_2$ (446 nm), $^2F_5/_2$ (454 nm), $^4F_7/_2$ (491 nm),

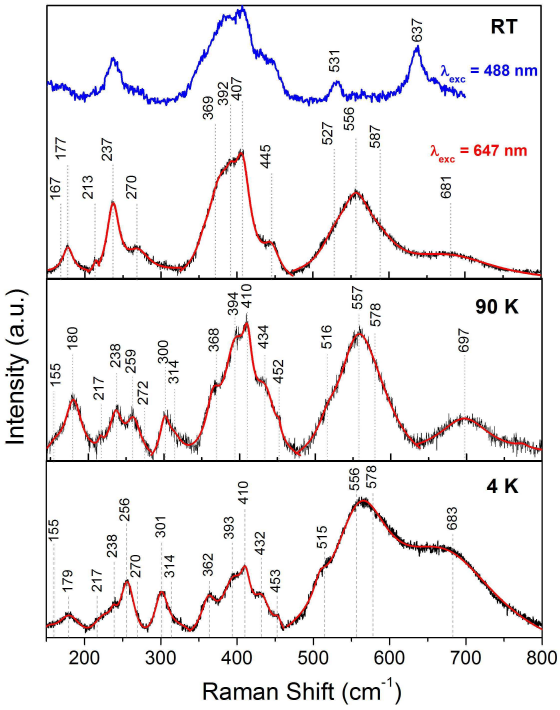

Figure 3: Measured (in black) and fitted (in red) Raman spectra of $LaGdO_3$ at room temperature (RT), 90 K and 4 K. The spectra were fitted to the sum of Lorentzian profiles centred around the indicated phonon frequency (in cm^{-1}). $\lambda_{laser} = 647$ nm. The Raman spectrum taken with $\lambda_{laser} = 488$ nm is shown on the top (in blue) for comparison purposes. Note that the broad bands between 500 and 800 cm^{-1} correspond to red luminescence coming from unintentional Er^{3+} impurities.

$^2H_{11}/_2$ (522 nm), $^4S_3/_2$ (547 nm), $^4F_9/_2$ (654 nm), $^4I_{11}/_2$ (979 nm) and $^4I_{13}/_2$ (1537 nm). The characteristic absorption peak of Yb^{3+} corresponds to the $^2F_{7/2} \rightarrow ^2F_{5/2}$ transition and is located at 977 nm. All peak positions and band widths are comparable with standard Er^{3+} and Er^{3+}/ Yb^{3+} spectra in other host materials.[33,34]

RT PL spectra, as a function of Er^{3+} and Er^{3+}/Yb^{3+} doping concentration, of $LaGdO_3$: x% Er^{3+} (x = 0.1, 1, 2, 5) nanocrystals, were measured under 488 nm laser excitation (Fig.5). The PL spectra show mainly green and red emissions, which are associated with Er^{3+} transitions: $^2H_{11/2} \rightarrow ^4I_{15/2}$ (525 nm) and $^4S_{3/2} \rightarrow ^4I_{15/2}$ (549 nm), and $^4F_{9/2} \rightarrow ^4I_{15/2}$ (665 nm), respectively.

Upon blue excitation (488 nm) all samples show a strong green and red luminescence, except the Er^{3+}(0.1%)-doped sample, where the red luminescence is negligible in comparison

Table 2: Frequency of the observed phonon modes of $LaGdO_3$ (Monoclinic $C2/m$ phase) at 4 and 300 K by Raman spectroscopy, and their tentative assignment within the monoclinic structure following results given elsewhere.[17,32] *lum.* refers to luminescence peaks with emissions at 671 and 677 nm coming from unintentional Er^{3+}– impurities. Raman peaks at 531 and 637 cm^{-1} were detected using λ_{laser}= 488 nm.

Phonon freq. (cm^{-1})		Assignment
4 K	300 K	
155	167	A_g
179	177	A_g
217	213	A_g
238	237	A_g
256		A_g
270	270	A_g
301		B_g
362	369	A_g
393	392	B_g
410	407	B_g *(+A_g?)*
432		B_g
	531	A_g
556	556	*lum.*
	637	A_g
683	681	*lum.*

to the green one. Importantly, green luminescence is highly enhanced when increasing Er^{3+} concentration, with a maximum for $LaGdO_3$: 1% Er^{3+}. Red emission also increases with Er^{3+} content and reaches its maximum at 5 mole% Er^{3+} concentration. When increasing the doping concentrations above 1%, green luminescence decreases because of cross-relaxation processes among Er^{3+} ions are favored, and thus emission takes place from low-lying excited states. These processes do require overlap between emission and absorption bands between Er^{3+} neighbours and are governed by the Er^{3+}–Er^{3+} interaction, both being very sensitive to Er^{3+}–Er^{3+} distances, *i.e.* Er^{3+} concentration within a statistical distribution.[35]

The knowledge of the critical Er^{3+} concentration for each host lattice is crucial to improve PL capabilities of the material for applications, particularly, in optical thermometry. Wang *et al.* showed that the temperature sensitivity of low concentrated Y_2O_3: Er^{3+} increases

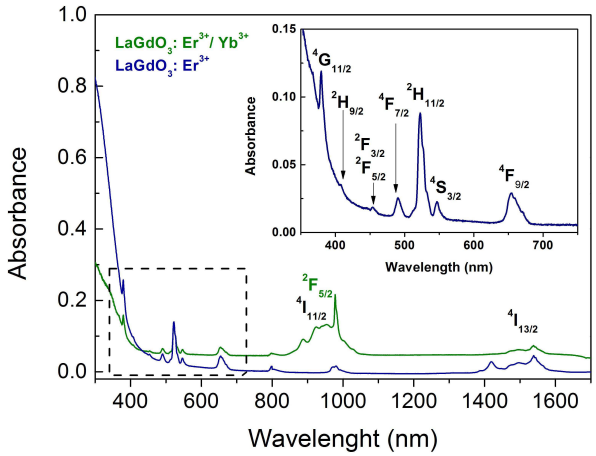

Figure 4: Absorption spectrum of 2% Er^{3+} and 2% Er^{3+}/20% Yb^{3+} doped $LaGdO_3$ in the UV-VIS-NIR region. Peak assignment corresponds to Er^{3+} excited levels (absorption from the $^4I_{15/2}$ ground state) –in black–, and Yb^{3+} excited level (absorption from the $^2F_{7/2}$ ground state) –in green–. Insert shows a magnification of the VIS region.

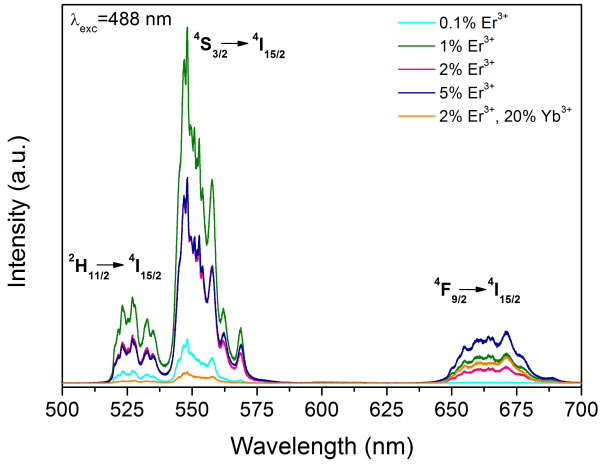

Figure 5: Luminescence spectra of $LaGdO_3$: x mole% Er^{3+} (x = 0.1, 1, 2, 5) at room temperature under 488 nm excitation.

almost twice the sensitivity of the same highly doped material.[20] Namely, they show that the optimum doping concentration for achieving best sensing capabilities is 1 mole% Er^{3+} in the mentioned lattice.

Upconversion PL and Lifetime

RT UC emission spectra of the Er^{3+}- and Er^{3+}/Yb^{3+}-doped $LaGdO_3$ samples under continuos wave (CW) 980 nm excitation are shown in Fig. 6.

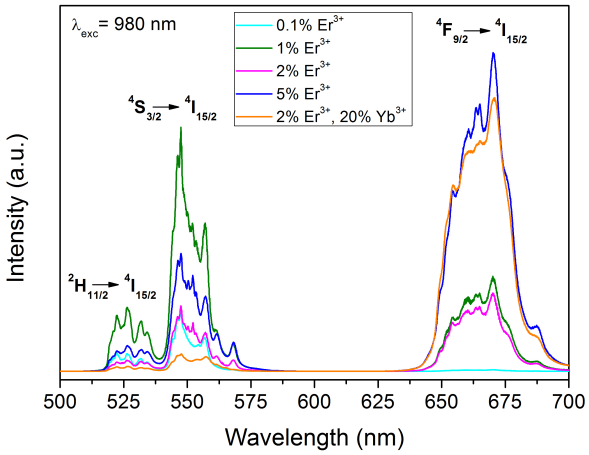

Figure 6: Luminescence spectra of $LaGdO_3$: $x\%$ Er^{3+} ($x = 0.1$, 1, 2, 5) at room temperature under CW 980 nm excitation.

The emission spectra of the $LaGdO_3$: $x\%$ Er^{3+} samples exhibit strong green and red emission bands, assigned to the $^2H_{11/2} \rightarrow {}^4I_{15/2}$ (525 nm), $^4S_{3/2} \rightarrow {}^4I_{15/2}$ (549 nm), and $^4F_{9/2} \rightarrow {}^4I_{15/2}$ (665 nm) transitions of Er^{3+}, respectively (Fig. 7), reaching the maximum UC emission for $LaGdO_3$: 1% Er^{3+}. In this case, UC is achieved partly by excited–state absorption (ESA) and partly by energy transfer upconversion (ETU). For low Er^{3+} concentrations we would expect that the GSA/ESA mechanism dominates whereas for highly doped samples the dominant UC mechanism is mainly GSA/ETU. However, this argument applies if we are dealing with Er^{3+} monomers but GSA/ETU mechanism can be efficient even for low Er^{3+} concentrations if the host lattice preferentially accommodates Er^{3+} in pairs (dimers).

When exploring shorter wavelengths, we do also observe UC emission bands, associated with transitions: $^4G_{11/2} \rightarrow {}^4I_{15/2}$ (383 nm), $^2H_{9/2} \rightarrow {}^4I_{15/2}$ (410 nm), $^4F_{3/2} \rightarrow {}^4I_{15/2}$ (446 nm), $^4F_{5/2} \rightarrow {}^4I_{15/2}$ (457 nm) and $^4F_{7/2} \rightarrow {}^4I_{15/2}$ (492 nm), such as Fig. 8 shows. Interestingly, the Er^{3+}/Yb^{3+} doped sample shows strong UV/blue luminescence under IR excitation compared to the Er^{3+}-doped sample, pointing out the relevance of Yb^{3+} in the UC luminescence.

In general, UC processes involving Er^{3+}- and Er^{3+}/Yb^{3+}-doped materials under IR excitation are well-known as it has attracted solid-state spectroscopists due to potential application in sensing and as IR-to-VIS converters. These systems have been even more investigated in the framework of nanoscience and nanotechnology due its enormous potential for disruptive

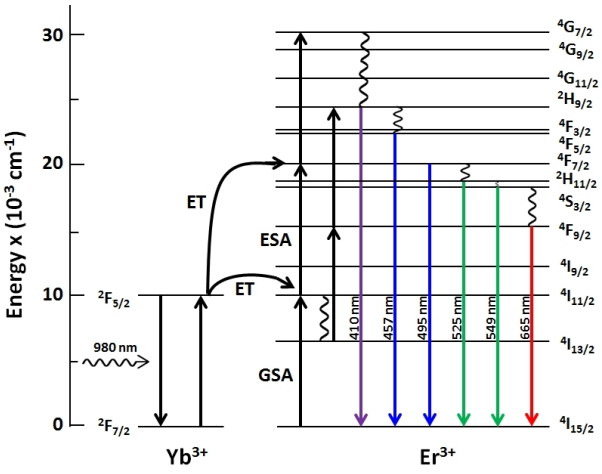

Figure 7: Mechanism of the upconversion processes in Er^{3+} and Er^{3+}/Yb^{3+} doped $LaGdO_3$ nanocrystals following 980 nm excitation. The colored solid arrows represent the upconverted radiative emissions, while curly lines represent non-radiative decays. Black arrows represent excitation processes. For simplicity some mechanisms and arrows have been omitted.

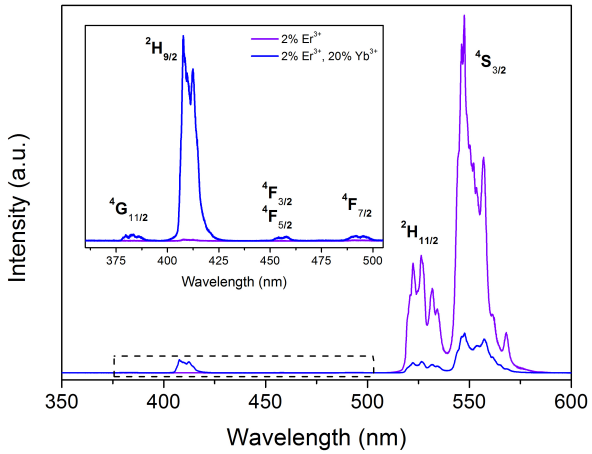

Figure 8: Luminescence spectra of $LaGdO_3$: 2% Er^{3+} and $LaGdO_3$: 2% Er^{3+}, 20% Yb^{3+} at room temperature under CW 980 nm excitation. Energy levels involved in the transitions from the excited states to the $^4I_{15/2}$ ground state are labeled in black.

applications beyond materials science. Biosensing, biomedical and wide-use thermometry applications are well-known examples.

In the case of Er^{3+}/Yb^{3+} co-doped samples, it has been established that energy transfer upconversion (ETU) governs the UC luminescence, due, first, to the large absorption cross-section of Yb^{3+} ions compared to Er^{3+} when exciting with 980 nm photons, and, second, to the excellent matching resonance between the Yb^{3+} absorption and two– and three–photon

absorption of Er^{3+} excited states.[36] Both characteristics make these two coupled ions an ideal system for UC phenomena. These processes are also favored for high doping concentrations of Er^{3+}.

Focusing on the thermometric properties, the population of thermalized $^2H_{11/2}$ and $^4S_{3/2}$ excited states of Er^{3+} is due to either a process by which two excited nearby Yb^{3+} transfer simultaneously or sequentially the excitation to the excited state of Er^{3+}, or, more efficiently, via two photon absorption – one exciting one Yb^{3+} and the neighbour Er^{3+} followed by a non-radiative energy transfer (GSA/ETU) from Yb^{3+} to Er^{3+}.[37]

These mechanisms are likely responsible for UC in the investigated material, and both allow population of the excited level $^4F_{7/2}$ of Er^{3+} upon IR excitation. Nevertheless, the latter mechanism is known to govern the UC process in Er^{3+}, Yb^{3+}-codoped materials[38] and is also the main mechanism in Er^{3+}, Yb^{3+}-codoped $LaGdO_3$, resulting in the VIS emissions at 525 nm and 549 nm (green) and 670 nm (red). The thermometry basis lies on the thermal equilibrium population of the $^2H_{11/2}$ and $^4S_{3/2}$ excited states, which allows us to determine the temperature from their relative emission intensities ($FIR = I_{525}/I_{549}$) and their energy separation, ΔE, that can be spectroscopically determined from the corresponding emission peak positions. In order to elucidate the role played by each UC mechanism, time-resolved spectroscopy is a suitable technique as these processes exhibit a different excited state dynamics.

The time-dependence fluorescence decay curves $I(t)$ of $^4S_{3/2}$ and $^4F_{9/2}$ levels of Er^{3+}, for the $LaGdO_3$: 1% Er^{3+} nanocrystals, are shown in Fig. 9. Besides the time-dependence behavior, $I(t)$ provides the average lifetime parameter defined as:

$$<\tau>=\frac{\int I(t)\,t\,dt}{\int I(t)\,dt} \tag{2}$$

which gives an useful information on the de-excitation process efficiency. Table 3 collects the mean emission lifetimes of all the synthesized samples. It must be noted that $<\tau>$ for

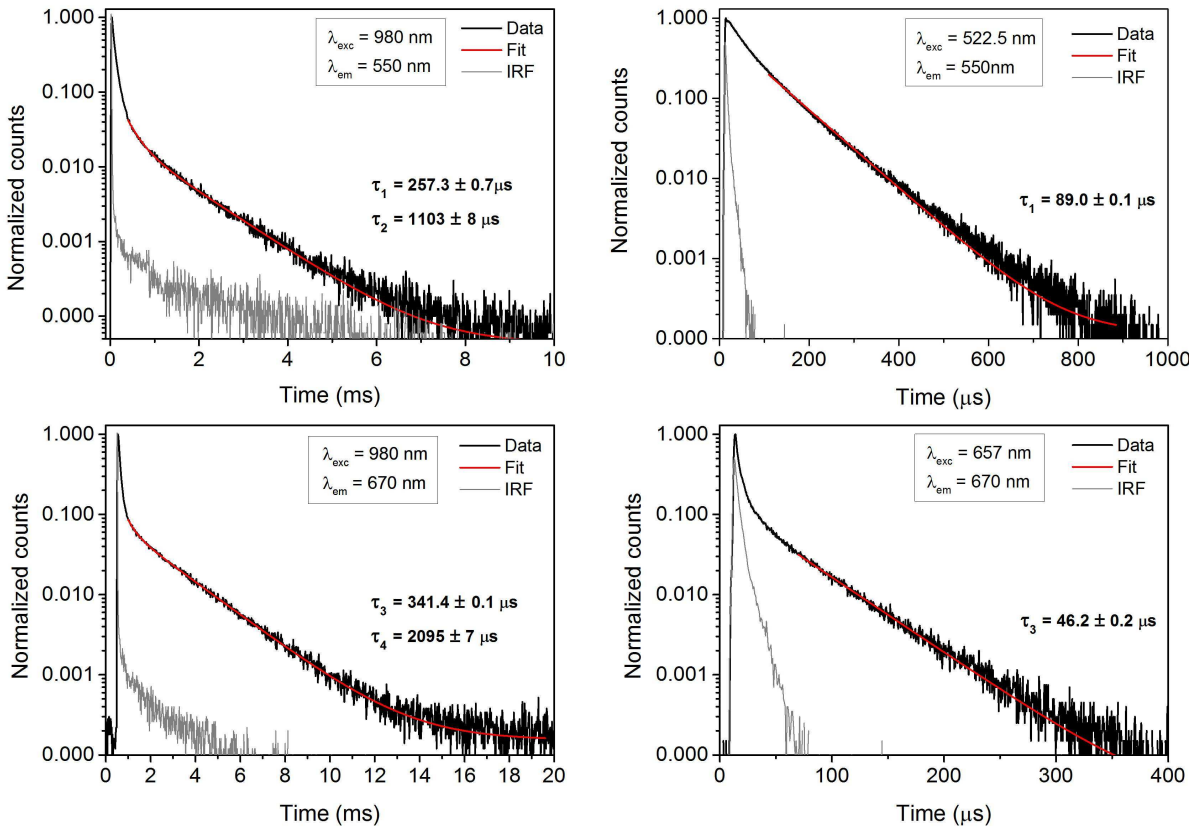

Figure 9: Fluorescence lifetime of $LaGdO_3$: 1% Er^{3+} at room temperature under VIS and IR excitations after μs pulses excitation with a 980 nm laser and a Xe lamp.

Table 3: Fluorescence lifetime of $LaGdO_3$: x% Er^{3+} (x=0.1, 1, 2, 5) under IR and VIS excitation.

Sample	λ_{exc} = 980 nm λ_{em} = 550 nm	λ_{exc} = 522.5 nm λ_{em} = 550 nm	λ_{exc} = 980 nm λ_{em} = 670 nm	λ_{exc} = 657 nm λ_{em} = 670 nm
0.1% Er^{3+}	$\tau_1 = 144.5 \pm 0.1\,\mu s$ $\tau_2 = 944 \pm 7\,\mu s$ $<\tau> = 489\ \mu s$	$\tau_1 = 128.7 \pm 0.1\,\mu s$	$\tau_3 = 142.5 \pm 0.2\,\mu s$ $\tau_4 = 1574 \pm 3\,\mu s$ $<\tau> = 621\ \mu s$	$\tau_3 = 50.6 \pm 0.3\,\mu s$
1% Er^{3+}	$\tau_1 = 257.3 \pm 0.7\,\mu s$ $\tau_2 = 1103 \pm 8\,\mu s$ $<\tau> = 922\ \mu s$	$\tau_1 = 89.0 \pm 0.1\,\mu s$	$\tau_3 = 341.4 \pm 0.1\,\mu s$ $\tau_4 = 2095 \pm 7\,\mu s$ $<\tau> = 1975\ \mu s$	$\tau_3 = 46.2 \pm 0.2\,\mu s$
2% Er^{3+}	$\tau_1 = 133.4 \pm 0.7\,\mu s$ $\tau_2 = 1022 \pm 1\,\mu s$ $<\tau> = 863\ \mu s$	$\tau_1 = 63.6 \pm 0.1\,\mu s$	$\tau_3 = 93.6 \pm 0.6\,\mu s$ $\tau_4 = 1950 \pm 2\,\mu s$ $<\tau> = 1720\ \mu s$	$\tau_3 = 40.6 \pm 0.8\,\mu s$
5% Er^{3+}	$\tau_1 = 165.4 \pm 0.2\,\mu s$ $\tau_2 = 1026 \pm 2\,\mu s$ $<\tau> = 918\ \mu s$	$\tau_1 = 36.4 \pm 0.2\,\mu s$	$\tau_3 = 4.4 \pm 0.2\,\mu s$ $\tau_4 = 1810 \pm 2\,\mu s$ $<\tau> = 1809\ \mu s$	$\tau_3 = 25.3 \pm 0.3\,\mu s$

Table 4: Fluorescence lifetime of $^4I_{11/2}$ state in $LaGdO_3$: x% Er^{3+} under IR excitation.

Sample	λ_{exc} = 968 nm λ_{em} = 980 nm
1% Er^{3+}	$\tau_1 = 2277.6 \pm 0.1\,\mu s$
2% Er^{3+}	$\tau_1 = 2236.8 \pm 0.1\,\mu s$
5% Er^{3+}	$\tau_1 = 2107.8 \pm 0.4\,\mu s$

UC-induced luminescence was found to be maximum for the 1% Er^{3+} doped sample, where $<\tau>$ ($^4S_{3/2}$) = 922 μs and $<\tau>$ ($^4F_{9/2}$) = 1975 μs. Nevertheless, these $<\tau>$ values contrast with those measured under direct VIS excitation, which are shorter than those measured via UC. $<\tau>$ progressively decreases with increasing Er^{3+} concentration from 129 μs (0.1 mole%) to 36 μs (5 mole%) for the $^4S_{3/2}$ level, and from 50.6 to 25.3 μs for the $^4F_{9/2}$ level.

These lifetime values indicate that direct excitation upon the $^4S_{3/2}$ and $^4F_{9/2}$ excited states yields a relative rapid de-excitation, which slightly decrease with the increase in Er^{3+} concentration. However, $<\tau>$ increases by an order of magnitude (ms range) when excitation is accomplished by IR excitation through UC processes (Table 3). It means that the excited-state dynamics of $^4S_{3/2}$ and $^4F_{9/2}$ levels are mainly governed by the long-lived $^4I_{11/2}$ (2.3 ms) and $^4I_{13/2}$ (1.98 - 2.7 ms)[39,40] excited states that act as reservoirs. The measured lifetime associated with $^4I_{11/2}$ as a function of the Er^{3+} concentration are collected in Table 4. Interestingly, the $^4I_{11/2}$ emission lifetime is about 2.2 ms, independently of the Er^{3+} content. Therefore, the slow depopulation dynamics of these states controls the population feeding rate of the higher-energy emitting levels, and thus their longer UC luminescence lifetime. It is worthwhile to note that the UC green and red lifetimes, like the UC NIR lifetime, are practically unaffected by the Er^{3+} concentration thus making it attractive to use in PL efficient materials requiring high doping concentrations. Given that the UC mechanism involves likely GSA/ETU, the higher the Er^{3+} concentration (or Yb^{3+} in doubly doped

Er^{3+}, Yb^{3+} systems), the larger number of nearby Er^{3+} (or Yb^{3+}), the higher UC excited-state population governing the de-excitation dynamics of visible emissions. Besides, the slight Er^{3+} concentration dependence of the UC-induced lifetime suggests that $LaGdO_3$ is probably a suitable host matrix to accommodate Er^{3+} dopant preferentially in pairs. In fact, the similitude between ionic radii of La^{3+} and Gd^{3+} favors these two sites to be preferentially occupied by Er^{3+} forming pairs. This allows us explaining why GSA/ETU mechanisms are efficient even for low doping concentrations in singly Er^{3+}-doped material.

To validate this model we have investigated the mechanism behind UC processes in $LaGdO_3$: 1% Er^{3+} and $LaGdO_3$: 2% Er^{3+}, 20% Yb^{3+}, through the intensity dependence of the emissions at 410, 549 and 670 nm with the pumping power of the 980 nm laser. For low pump powers, the UC emission intensity (I_{UC}) is expected to be proportional to the IR excitation intensity (I_{IR}) through the number of photons involved in the process (n) as follows:[41,42]

$$I_{UC} \propto {I_{IR}}^n \tag{3}$$

However, other exponents ($n < 3$) may appear depending on the pumping power and the relative rates for excited-state de-excitation into other low energy levels, and excitation of higher energy levels via ETU, the latter being strongly affected by the sensitizer and acceptor concentrations, unless the host matrix provides preferential sites for pair formation. In ETU processes, involving low de-excitation rates and highly population of excited sensitizers, exponents close to 1 can be observed at moderate and high excitation powers.[41] Figure 10 shows the log–log plot of UC emission intensities as a function of the laser pumping power for UV-blue (410 nm), green (525 + 549 nm) and red (665 nm) emissions in $LaGdO_3$: 1% Er^{3+} and $LaGdO_3$: 2% Er^{3+}, 20% Yb^{3+}. For increasing pump powers in the 1% Er^{3+}–doped sample, GSA/ETU is the dominant mechanism and the saturation of the UC emission is related to the depletion of intermediate excited states that act as reservoirs for the UC

process. The relative low concentration of Er^{3+} (acting as sensitizer and acceptor at the same time) favors a lower de-excitation rate by energy transfer. By contrast, this rate increases for high concentration of sensitizer (*i.e.* Yb^{3+}). The average lifetime of direct-excitation-induced green and red emissions decreases with Er^{3+} concentration thus supporting this view. In the intermediate region, the intensity vs. pump powers is a competition between linear decay and UC, and the luminescence exhibits slopes that are between the two limiting cases.[41]

The n values found in Yb^{3+}(20%), Er^{3+} (2%) being slightly higher than for Er^{3+} (1%) highlights the relevance of the concentration. In particular, the increase of de-excitation rate to lower energy levels in the 5% Er^{3+} doped material is evidenced through the relative enhancement of the UC red and green emission with respect to blue emission, in comparison with the less doped material, which relative blue-to-green-to-red emission increases dramatically (Fig. 6). Therefore, increasing dopant concentration yields higher n exponents of the pump power I_{UC} *vs.* I_{IR} dependence (Eq. 3). Indeed, the fitting of data to eq. 3 reveals slopes of 1.9 ± 0.1 for $^4F_{9/2}$, 1.5 ± 0.1 for $^4S_{3/2}$ and 1.6 ± 0.1 for $^2H_{9/2}$ emitting states in $LaGdO_3$: 1% Er^{3+} in the low pump power regime, whereas they are 2.2 ± 0.2, 1.9 ± 0.2 and 2.3 ± 0.2, respectively, in $LaGdO_3$: 2% Er^{3+}, 20% Yb^{3+}, what is in accordance with the proposed UC mechanisms shown in Fig.7. This different pumping power dependence of the Er^{3+}-doped and Yb^{3+}, Er^{3+}-doubly doped $LaGdO_3$ is noteworthy. It is worth mentioning that deviations of n from the ideal n= 3 value is not related to the powdered sample. Although it is well known that the grain structure and sample compaction can affect the UC emission efficiency by decreasing it at the nanoscale down to 20%,[43] we have verified that this effect does not affect its power dependence. The measured n values of Fig. 10 are the same for diluted powdered and compacted samples, thus confirming that the variability of n mainly rely on the host matrix structure and relative dopant concentrations.

Regarding the $LaGdO_3$: 2% Er^{3+}, 20% Yb^{3+} sample, it must be noted that the UC intensity vs. pump power in the high-power limit approaches a slope of 1 in the log–log plot for any emission band of Er^{3+}, regardless of the number of excitations and involved energy

steps.[42]

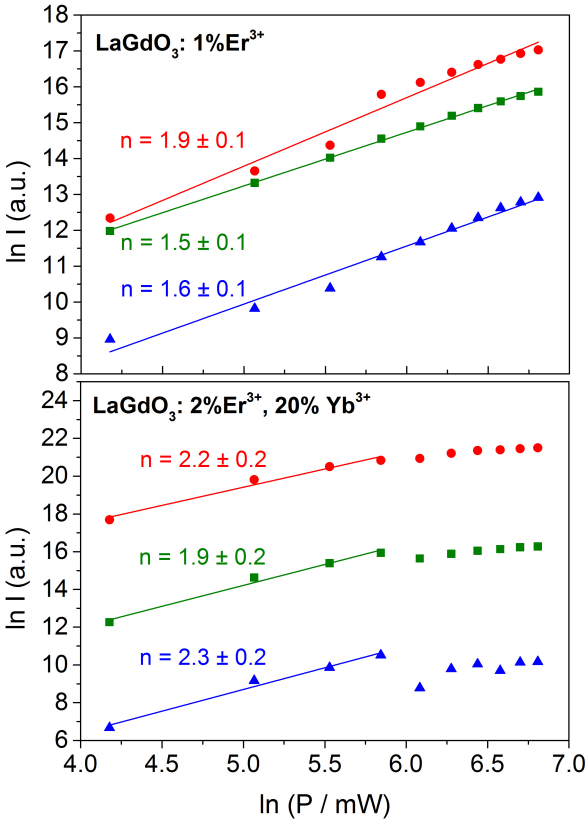

Figure 10: UC emission intensities as a function of the logarithm of the laser pumping power for UV-blue (410 nm), green (549 nm) and red (665 nm) emissions in $LaGdO_3$: 2% Er^{3+}, 20% Yb^{3+}.

Temperature-dependent PL

Figures 11a and 11b show the PL spectra of 1% Er^{3+} doped $LaGdO_3$ nanocrystals in the green spectral region as a function of temperature (298-873 K) under CW 488 nm laser excitation. The green emission consists of several bands between 515 and 570 nm corresponding to transitions between $^2H_{11/2}$ and $^4S_{3/2}$ excited states to the $^4I_{15/2}$ ground state of Er^{3+}, respectively. As these two excited states are thermally coupled, their emission intensity ratio, *FIR*, depends on the respective excited-state equilibrium populations, which are governed by the Boltzmann distribution factor:[44]

$$FIR = \frac{I_{525}}{I_{549}} = C\, e^{-\Delta E/kT} \quad (4)$$

where I_{525} and I_{549} are the integrated intensities of the two thermally-coupled multiplets, C is a constant that depends on the state degeneracy, spontaneous emission rate, and photon energies of the emitting states in the host material,[45] ΔE is the energy gap between the $^2H_{11/2}$ and $^4S_{3/2}$ multiplets, –both C and ΔE are characteristic of each material host–, k is the Boltzmann constant, and T is the absolute temperature.

The temperature dependence of the luminescence can be easily obtained by least-square fitting of the experimental $\ln(FIR)$ vs. $1/T$ data to a linear equation, the slope of which gives $\Delta E/k$ and the $\ln(FIR)$-intercept, $\ln(C)$ (Eq.4). These two parameters provide the thermometric scale (Fig. 11c) with values of ΔE = 1052.9 K = 737 ± 5 cm^{-1} (91.4 ± 0.9 meV) and C = 8.25 ± 0.12. The so-obtained energy gap coincides with that measured spectroscopically from the $^2H_{11/2}$ and $^4S_{3/2}$ centroid positions. Due to the weak crystal-field dependence of these transitions, the obtained gap in $LaGdO_3$: Er^{3+} is also comparable to that obtained in other reported compounds like fluorotellurite glass doped with Er^{3+} (810 cm^{-1}),[46] $LiNbO_3$:Er^{3+}/Yb^{3+} (860 cm^{-1})[47] and $NaY(MoO_4)_2$: Er^{3+}/Yb^{3+} (736 cm^{-1}),[48] or $NaYF_4$: Er^{3+}/Yb^{3+} (714 cm^{-1}).[11]

To better illustrate the suitability of 1% Er^{3+}-doped $LaGdO_3$ nanopowders as sensor for optical thermometry, its performance and temperature range of operation with different Er^{3+}-based host materials is evaluated through their absolute (S) and relative (S_R) sensitivities. These parameters can be deduced from eq. (4) as:

$$S = \left|\frac{\partial FIR}{\partial T}\right| = FIR\,\frac{\Delta E}{kT^2} \quad (5)$$

$$S_R = \left|\frac{1}{FIR}\frac{\partial FIR}{\partial T}\right| = \frac{\Delta E}{kT^2} \quad (6)$$

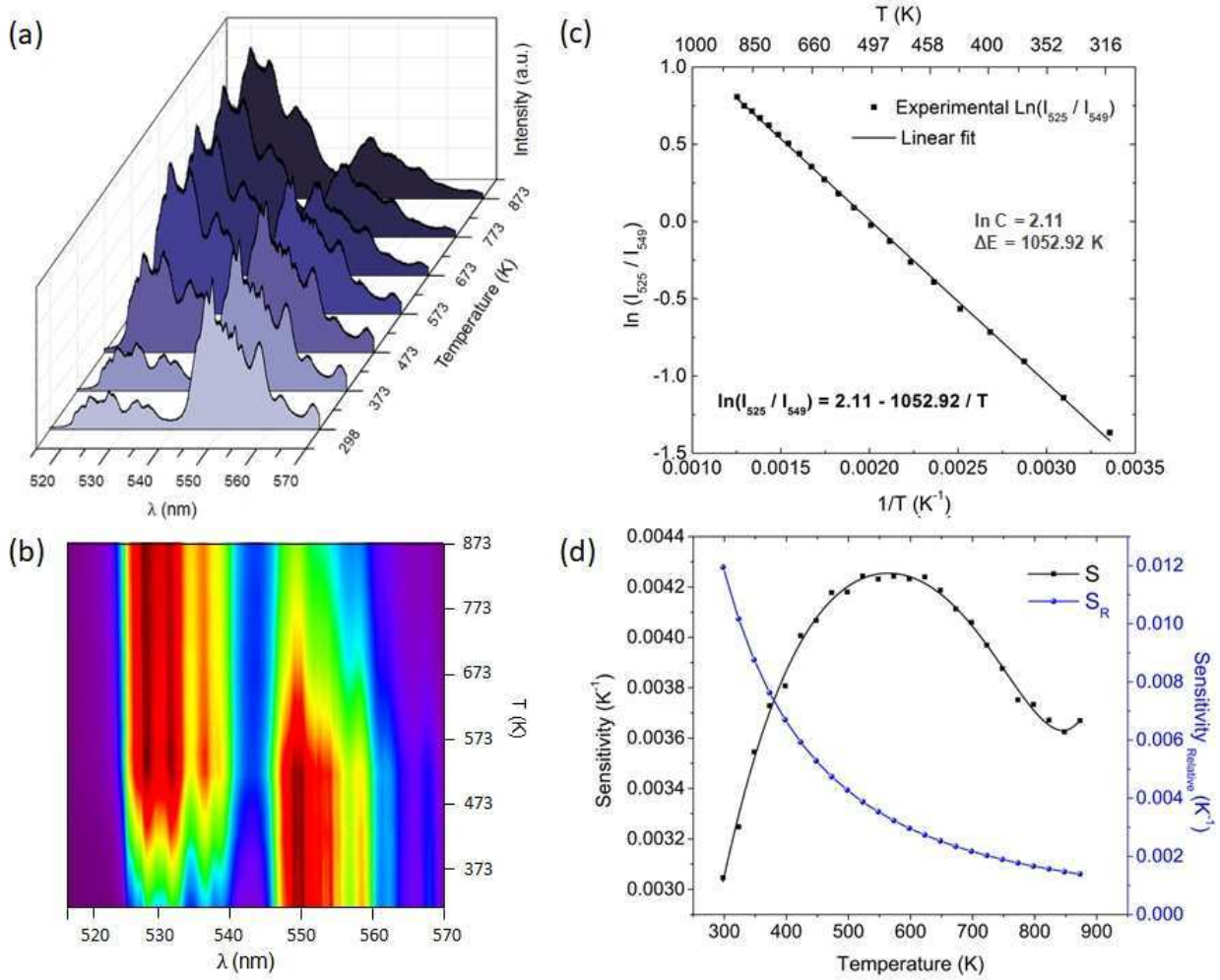

Figure 11: Temperature sensing properties of 1% Er^{3+}-doped $LaGdO_3$ nanopowders under λ=488 nm excitation. (a) Emission spectra as a function of the absolute temperature; (b) intensity contour plots of the emission spectra at different temperatures; (c) log plot of the *FIR* as a function of the reciprocal temperature; (d) sensor absolute -black- and relative -blue- sensitivities as a function of temperature.

For accurate nanosensing S values as large as possible are desired. Since $S \approx e^{-\Delta E/kT}$ the energy gap limits the ratiometric sensitivity for biomedical purposes but it is an excellent system for measuring temperature in industrial environments where accurate measurements at high temperature are necessary.

The obtained values for 1% Er^{3+}-doped $LaGdO_3$ are shown in Fig. 11d as a function of temperature. The highest sensitivity is found at T = 554 K with $S = 4.3{\cdot}10^{-3}$ K^{-1}, while the highest relative sensitivity S_R is at 0 K and decreases with temperature, reaching a value

of $1.2{\cdot}10^{-2}$ K^{-1} at 298 K and $0.1{\cdot}10^{-2}$ K^{-1} at 900 K. Table 5 collects sensitivity values and temperature range for the most suitable Er^{3+}-based optical thermometer materials. It is worth noting that the sensor sensitivity S reported here for $LaGdO_3$ is significantly higher than that reported by Siaï *et al.* for the same host material ($3.4 \cdot 10^{-3}$ K^{-1} at 393 K).[15] This efficiency enhancement is attributed to the optimization of Er^{3+} concentration we performed in the sol-gel-Pechini synthesized monoclinic single phase of $LaGdO_3$ matrix. The achieved sensitivity with this method is comparable to the best sensitivities attained in other Er^{3+}-based materials, as for instance $NaY(WO_4)_2$ (see Table 5). Interestingly, this host material provides one of the largest-ever temperature ranges of operation.

Table 5: Comparison of thermometric properties in Er^{3+}/Yb^{3+}-doped luminescent materials: absolute sensitivity and temperature range of operation. The maximum sensitivity temperature is shown in parenthesis.

Sensing material	S $\cdot 10^{-3}$ (K^{-1})	Temperature range (K)	Reference
$LaGdO_3$: 1% Er^{3+}	4.3 (554 K)	298-873	This work
$LaGdO_3$: Er^{3+}/Yb^{3+}	3.4 (393 K)	283-393	[15]
Gd_2O_3: Er^{3+}/Yb^{3+}	3.9 (300 K)	300-900	[49]
ZnO: Er^{3+}	6.2 (443 K)	273-573	[50]
$SrSnO_3$: Er^{3+}	7.9 (368 K)	294-372	[51]
$NaYF_4$: Er^{3+}/Yb^{3+}	2.4 (554 K)	300-700	[52]
$Yb_2Ti_2O_7$: Er^{3+}	7.4 (340 K)	290-610	[53]
Fluorotellurite glass: Er^{3+}	8.0 (541 K)	100–573	[54]
Silicate glass: Er^{3+}/Yb^{3+}	3.1 (550 K)	300–700	[55]
$Y_3Al_5O_12$ (YAG): Er^{3+}/Yb^{3+}	1.7 (404 K)	298–573	[56]
$BaTiO_3$: Er^{3+}/Yb^{3+}	1.9 (410 K)	120–505	[57]
$NaY(WO_4)_2$: Er^{3+}/Yb^{3+}	15.5 (530 K)	298–700	[58]

Conclusions

We have shown that Er^{3+}-doped $LaGdO_3$ exhibits suitable sensing figures for using as an optical nanothermometer in the monoclinic phase B for Er^{3+} concentration of 1 mole%. The massive stabilization of this phase under severe RE^{3+} doping conditions has been possible through the sol–gel Pechini method. The temperature range of operation of $LaGdO_3$ is one of

the largest-ever found. $LaGdO_3$ host is worth for thermometry since it shows better UC green emission efficiencies using singly Er^{3+}-doped materials in contrast to Er^{3+},Yb^{3+}-codoped materials usually employed in UC-related thermometry. This finding makes $LaGdO_3$ a specially well suited host for nanothermometry using less than an order of magnitude of RE^{3+} impurity content. In addition, this material is suitable for biosensing as thermometry can be achieved via UC luminescence and it does not matter the excitation way for the temperature calibration. This allows thermometry by IR excitation in a biocompatible host. We have also demonstrated that UC is mainly induced by a GSA/ETU mechanism, thus requiring to increase the Yb concentration up to 20 mole% in order to get suitable luminescence efficiencies for optical thermometry, keeping the same monoclinic type B structure of the host material. We suggested that $LaGdO_3$ structure is well suited to favor Er-Er pair formation, and thus providing UC capabilities for low Er^{3+} concentrations. We have shown that decreasing dopant concentration, using Er^{3+}-doped $LaGdO_3$ below 2 mole%, largely enhances the relative green luminescence with respect to red luminescence, even more using direct excitation instead of UC excitation, what is of interest for high temperature sensing.

Acknowledgement

This work has been supported by the Spanish Ministerio de Economía, Industria y Competitividad (Projects Nos. MAT2015-69508-P and PGC2018-101464-B-I00), the European Research Council (Ref. NCLas H2020-EU829161), and BSH Electrodomésticos España, S.A.

References

(1) Scheps, R. Upconversion laser processes. *Progress in Quantum Electronics* **1996**, *20*, 271–358.

(2) Phillips, M. L. F.; Hehlen, M. P.; Nguyen, K.; Sheldon, J. M.; Cockroft, N. J. Upcon-

version phosphors: recent advances and new applications. Physics and Chemistry of Luminescent Materials: Proceedings of the Eighth International Symposium. 2000; p 123.

(3) Mi, C.; Tian, Z.; Cao, C.; Wang, Z.; Mao, C.; Xu, S. Novel microwave-assisted solvothermal synthesis of $NaYF_4$: Yb, Er upconversion nanoparticles and their application in cancer cell imaging. *Langmuir* **2011**, *27*, 14632–14637.

(4) Qian, L. P.; Zhou, L. H.; Too, H. P.; Chow, G. M. Gold decorated $NaYF_4$: Yb, Er/$NaYF_4$/silica (core/shell/shell) upconversion nanoparticles for photothermal destruction of BE(2)-C neuroblastoma cells. *Journal of Nanoparticle Research* **2011**, *13*, 499–510.

(5) Xu, J.; Gulzar, A.; Liu, Y.; Bi, H.; Gai, S.; Liu, B.; Yang, D.; He, F.; Yang, P. Integration of IR-808 sensitized upconversion nanostructure and MoS_2 nanosheet for 808 nm NIR light triggered phototherapy and bioimaging. *Small* **2017**, *13*, 1701841.

(6) Chen, C.; Liu, J.; Chen, Y.; Li, C.; Liu, X.; Huang, H.; Liang, C.; Lou, Y.; Shi, Z.; Feng, S. Sub-10 nm Sr_2LuF_7: Yb/Er@ Sr−2GdF7@ SrF_2 Up-Conversion Nanocrystals for Up-Conversion Luminescence–Magnetic Resonance–Computed Tomography Trimodal Bioimaging. *ACS applied materials & interfaces* **2017**, *9*, 5748–5756.

(7) Li, X.; Cao, J.; Hu, F.; Wei, R.; Guo, H. Transparent $Na_5Gd_9F_{32}$: Er^{3+} glass-ceramics: enhanced up-conversion luminescence and applications in optical temperature sensors. *RSC Advances* **2017**, *7*, 35147–35153.

(8) Zhang, A.; Sun, Z.; Liu, G.; Fu, Z.; Hao, Z.; Zhang, J.; Wei, Y. Ln^{3+} (Er^{3+}, Tm^{3+} and Ho^{3+})-doped NaYb $(MoO_4)_2$ upconversion phosphors as wide range temperature sensors with high sensitivity. *Journal of Alloys and Compounds* **2017**, *728*, 476–483.

(9) Jaque, D.; Vetrone, F. Luminescence nanothermometry. *Nanoscale* **2012**, *4*, 4301–4326.

(10) Ragan, D. D.; Gustavsen, R.; Schiferl, D. Calibration of the ruby R1 and R2 fluorescence shifts as a function of temperature from 0 to 600 K. *Journal of applied physics* **1992**, *72*, 5539–5544.

(11) Vetrone, F.; Naccache, R.; Zamarrón, A.; Juarranz de la Fuente, A.; Sanz-Rodríguez, F.; Martínez Maestro, L.; Martín Rodríguez, E.; Jaque, D.; García Solé, J.; Capobianco, J. A. Temperature sensing using fluorescent nanothermometers. *ACS nano* **2010**, *4*, 3254–3258.

(12) Xu, M.; Zou, X.; Su, Q.; Yuan, W.; Cao, C.; Wang, Q.; Zhu, X.; Feng, W.; Li, F. Ratiometric nanothermometer in vivo based on triplet sensitized upconversion. *Nature communications* **2018**, *9*, 2698.

(13) Mohanty, S. K.; Reinscheid, R. K.; Liu, X.; Okamura, N.; Krasieva, T. B.; Berns, M. W. In-depth activation of channelrhodopsin 2-sensitized excitable cells with high spatial resolution using two-photon excitation with a near-infrared laser microbeam. *Biophysical journal* **2008**, *95*, 3916–3926.

(14) Geitenbeek, R. G.; Prins, P. T.; Albrecht, W.; van Blaaderen, A.; Weckhuysen, B. M.; Meijerink, A. $NaYF_4$: Er^{3+}, Yb^{3+}/SiO_2 core/shell upconverting nanocrystals for luminescence thermometry up to 900 K. *The Journal of Physical Chemistry C* **2017**, *121*, 3503–3510.

(15) Siaï, A.; Haro-González, P.; Naifer, K. H.; Férid, M. Optical temperature sensing of Er^{3+}/Yb^{3+} doped $LaGdO_3$ based on fluorescence intensity ratio and lifetime thermometry. *Optical Materials* **2018**, *76*, 34–41.

(16) Wenhui, S.; Daiming, W. U.; Xiaoyuan, L. I.; Xianfeng, M. A.; Jianshi, Z.; Zhengnan, Q.; Yifeng, W.; Weina, L.; Zhongjiu, G. E. An investigation using high-pressure synthesis of double-rare-earth oxides of ABO_3-composition. *Physica B+ C* **1986**, *139*, 658–660.

(17) Pavunny, S. P.; Kumar, A.; Misra, P.; Scott, J. F.; Katiyar, R. S. Properties of the new electronic device material $LaGdO_3$. *physica status solidi (b)* **2014**, *251*, 131–139.

(18) Renero-Lecuna, C.; Martín-Rodríguez, R.; Valiente, R.; González, J.; Rodríguez, F.; Kramer, K. W.; Güdel, H. U. Origin of the high upconversion green luminescence efficiency in β-$NaYF_4$: 2% Er^{3+}, 20% Yb^{3+}. *Chemistry of materials* **2011**, *23*, 3442–3448.

(19) Shang, Y.; Hao, S.; Liu, J.; Tan, M.; Wang, N.; Yang, C.; Chen, G. Synthesis of up-conversion β-$NaYF_4$: Nd^{3+}/Yb^{3+}/Er^{3+} particles with enhanced luminescent intensity through control of morphology and phase. *Nanomaterials* **2015**, *5*, 218–232.

(20) Wang, R.; Zhang, X.; Liu, F.; Chen, Y.; Liu, L. Concentration effects on the FIR technique for temperature sensing. *Optical Materials* **2015**, *43*, 18–24.

(21) Costa, G. A.; Artini, C.; Ubaldini, A.; Carnasciali, M. M.; Mele, P.; Masini, R. Phase stability study of the pseudobinary system Gd_2O_3–Nd_2O_3 (T = 1350 ^{o}C). *Journal of Thermal Analysis and Calorimetry* **2008**, *92*, 101–104.

(22) Goldschmidt, V. M. Die gesetze der krystallochemie. *Naturwissenschaften* **1926**, *14*, 477–485.

(23) Artini, C.; Costa, G. A.; Carnasciali, M. M.; Masini, R. Stability field and structural properties of intra-rare earth perovskites. *Journal of Alloys and Compounds* **2010**, *494*, 336–339.

(24) Chi, Z. H.; You, S. J.; Yang, L. X.; Chen, L. C.; Jin, C. Q.; Wang, X. H.; Chen, R. Z.; Li, L. T.; Li, Y. C.; Li, X. D. et al. Structural stability of multiferroics $BiMnO_3$ under high pressure. *Journal of Electroceramics* **2008**, *21*, 863–866.

(25) Haumont, R.; Bouvier, P.; Pashkin, A.; Rabia, K.; Frank, S.; Dkhil, B.; Crichton, W. A.;

Kuntscher, C. A.; Kreisel, J. Effect of high pressure on multiferroic $BiFeO_3$. *Physical Review B* **2009**, *79*, 184110.

(26) Brites, C. D. S.; Martínez, E. D.; Urbano, R.; Rettori, C.; Carlos, L. A. D. Self–calibrated double luminescent thermometers through upconverting nanoparticles. *Frontiers in chemistry* **2019**, *7*, 267.

(27) Rodríguez-Carvajal, J. FULLPROF: a program for Rietveld refinement and pattern matching analysis. satellite meeting on powder diffraction of the XV congress of the IUCr. 1990.

(28) Hughes, I. D.; Däne, M.; Ernst, A.; Hergert, W.; Lüders, M.; Poulter, J.; Staunton, J. B.; Svane, A.; Szotek, Z.; Temmerman, W. M. Lanthanide contraction and magnetism in the heavy rare earth elements. *Nature* **2007**, *446*, 650.

(29) Seitz, M.; Oliver, A. G.; Raymond, K. N. The lanthanide contraction revisited. *Journal of the American Chemical Society* **2007**, *129*, 11153–11160.

(30) Shannon, R. D. Revised effective ionic radii and systematic studies of interatomic distances in halides and chalcogenides. *Acta crystallographica section A: crystal physics, diffraction, theoretical and general crystallography* **1976**, *32*, 751–767.

(31) Zarembowitch, J.; Gouteron, J.; Lejus, A. Raman spectrum of single crystals of monoclinic B-type gadolinium sesquioxide. *Journal of Raman Spectroscopy* **1980**, *9*, 263–265.

(32) Tompsett, G. A.; Phillips, R. J.; Sammes, N. M.; Cartner, A. M. Characterisation of $LaGdO_3$ by X-ray powder diffraction and Raman spectroscopy. *Solid state communications* **1998**, *108*, 655–660.

(33) Manzani, D.; da Silveira Petruci, J. F.; Nigoghossian, K.; Cardoso, A. A.; Ribeiro, S. J. L. A portable luminescent thermometer based on green up-conversion emission of Er^{3+}/Yb^{3+} co-doped tellurite glass. *Scientific reports* **2017**, *7*, 41596.

(34) Ajithkumar, G.; Yoo, B.; Goral, D. E.; Hornsby, P. J.; Lin, A.; Ladiwala, U.; Dravid, V. P.; Sardar, D. K. Multimodal bioimaging using a rare earth doped Gd_2O_2S: Yb/Er phosphor with upconversion luminescence and magnetic resonance properties. *Journal of Materials Chemistry B* **2013**, *1*, 1561–1572.

(35) Pisarski, W. A.; Pisarska, J.; Lisiecki, R.; Ryba-Romanowski, W. Sensitive optical temperature sensor based on up-conversion luminescence spectra of Er^{3+} ions in PbO–Ga_2O_3–XO_2 (X= Ge, Si) glasses. *Optical Materials* **2016**, *59*, 87–90.

(36) Pavani, K.; Kumar, J. S.; Srikanth, K.; Soares, M. J.; Pereira, E.; Neves, A. J.; Graça, M. P. F. Highly efficient upconversion of Er^{3+} in Yb^{3+} codoped non–cytotoxic strontium lanthanum aluminate phosphor for low temperature sensors. *Scientific reports* **2017**, *7*, 17646.

(37) Rodríguez, F.; Valiente, R.; Lavín, V.; Rodríguez-Mendoza, U. R. In *An introduction to high-pressure science and technology*; Recio, J. M., Menendez, J. M., De la Roza, A. O., Eds.; Boca Raton: CRC Press, 2016; Chapter 8, p 223.

(38) Auzel, F. Upconversion and anti-stokes processes with f and d ions in solids. *Chemical reviews* **2004**, *104*, 139–174.

(39) Choi, Y. G.; Kim, K. H.; Lee, B. J.; Shin, Y. B.; Kim, Y. S.; Heo, J. Emission properties of the Er^{3+}: 4I11/2→ 4I13/2 transition in Er^{3+}–and Er^{3+}/Tm^{3+}-doped Ge–Ga–As–S glasses. *Journal of non-crystalline solids* **2000**, *278*, 137–144.

(40) Martín-Rodríguez, R.; Fischer, S.; Ivaturi, A.; Froehlich, B.; Kramer, K. W.; Goldschmidt, J. C.; Richards, B. S.; Meijerink, A. Highly efficient IR to NIR upconversion in Gd_2O_2S: Er^{3+} for photovoltaic applications. *Chemistry of materials* **2013**, *25*, 1912–1921.

(41) Pollnau, M.; Gamelin, D. R.; Lüthi, S. R.; Güdel, H. U.; Hehlen, M. P. Power depen-

dence of upconversion luminescence in lanthanide and transition-metal-ion systems. *Physical Review B* **2000**, *61*, 3337.

(42) Suyver, J. F.; Aebischer, A.; García-Revilla, S.; Gerner, P.; Güdel, H. U. Anomalous power dependence of sensitized upconversion luminescence. *Physical Review B* **2005**, *71*, 125123.

(43) Wang, W.-N.; Widiyastuti, W.; Ogi, T.; Lenggoro, I. W.; Okuyama, K. Correlations between crystallite/particle size and photoluminescence properties of submicrometer phosphors. *Chemistry of Materials* **2007**, *19*, 1723–1730.

(44) Zhou, S.; Deng, K.; Wei, X.; Jiang, G.; Duan, C.; Chen, Y.; Yin, M. Upconversion luminescence of $NaYF_4$: Yb^{3+}, Er^{3+} for temperature sensing. *Optics Communications* **2013**, *291*, 138–142.

(45) León-Luis, S. F.; Monteseguro, V.; Rodríguez-Mendoza, U. R.; Rathaiah, M.; Venkatramu, V.; Lozano-Gorrín, A. D.; Valiente, R.; Muñoz, A.; Lavín, V. Optical nanothermometer based on the calibration of the Stokes and upconverted green emissions of Er^{3+} ions in $Y_3Ga_5O_{12}$ nano-garnets. *RSC Advances* **2014**, *4*, 57691–57701.

(46) León-Luis, S. F.; Rodríguez-Mendoza, U. R.; Martín, I. R.; Lalla, E.; Lavín, V. Effects of Er^{3+} concentration on thermal sensitivity in optical temperature fluorotellurite glass sensors. *Sensors and Actuators B: Chemical* **2013**, *176*, 1167–1175.

(47) Quintanilla, M.; Cantelar, E.; Cusso, F.; Villegas, M.; Caballero, A. C. Temperature sensing with up-converting submicron-sized $LiNbO_3$: Er^{3+}/Yb^{3+} particles. *Applied Physics Express* **2011**, *4*, 022601.

(48) Yang, X.; Fu, Z.; Yang, Y.; Zhang, C.; Wu, Z.; Sheng, T. Optical Temperature Sensing Behavior of High-Efficiency Upconversion: Er^{3+}–Yb^{3+} Co-Doped $NaY(MoO_4)_2$ Phosphor. *Journal of the American Ceramic Society* **2015**, *98*, 2595–2600.

(49) Singh, S. K.; Kumar, K.; Rai, S. B. Er^{3+}/Yb^{3+} codoped Gd_2O_3 nano-phosphor for optical thermometry. *Sensors and Actuators A: Physical* **2009**, *149*, 16–20.

(50) Wang, X.; Kong, X.; Yu, Y.; Sun, Y.; Zhang, H. Effect of annealing on upconversion luminescence of ZnO: Er^{3+} nanocrystals and high thermal sensitivity. *The Journal of Physical Chemistry C* **2007**, *111*, 15119–15124.

(51) Liu, G.; Fu, L.; Gao, Z.; Yang, X.; Fu, Z.; Wang, Z.; Yang, Y. Investigation into the temperature sensing behavior of Yb^{3+} sensitized Er^{3+} doped Y_2O_3, YAG and $LaAlO_3$ phosphors. *RSC Advances* **2015**, *5*, 51820–51827.

(52) Jiang, S.; Zeng, P.; Liao, L.; Tian, S.; Guo, H.; Chen, Y.; Duan, C.; Yin, M. Optical thermometry based on upconverted luminescence in transparent glass ceramics containing $NaYF_4$: Yb^{3+}/Er^{3+} nanocrystals. *Journal of Alloys and Compounds* **2014**, *617*, 538–541.

(53) Cao, B. S.; He, Y. Y.; Feng, Z. Q.; Li, Y. S.; Dong, B. Optical temperature sensing behavior of enhanced green upconversion emissions from Er–Mo: $Yb_2Ti_2O_7$ nanophosphor. *Sensors and Actuators B: Chemical* **2011**, *159*, 8–11.

(54) León-Luis, S. F.; Rodríguez-Mendoza, U. R.; Martín, I. R.; Lalla, E.; Lavín, V. Effects of Er^{3+} concentration on thermal sensitivity in optical temperature fluorotellurite glass sensors. *Sensors and Actuators B: Chemical* **2013**, *176*, 1167–1175.

(55) Zhou, S.; Li, C.; Liu, Z.; Li, S.; Song, C. Thermal effect on up-conversion in Er^{3+}/Yb^{3+} co–doped silicate glass. *Optical Materials* **2007**, *30*, 513–516.

(56) Liu, G.; Fu, L.; Gao, Z.; Yang, X.; Fu, Z.; Wang, Z.; Yang, Y. Investigation into the temperature sensing behavior of Yb^{3+} sensitized Er^{3+} doped Y_2O_3, YAG and $LaAlO_3$ phosphors. *RSC Advances* **2015**, *5*, 51820–51827.

(57) Mahata, M. K.; Koppe, T.; Mondal, T.; Brüsewitz, C.; Kumar, K.; Rai, V. K.; Hofsäss, H.; Vetter, U. Incorporation of Zn^{2+} ions into $BaTiO_3$: Er^{3+}/Yb^{3+} nanophosphor: an effective way to enhance upconversion, defect luminescence and temperature sensing. *Physical Chemistry Chemical Physics* **2015**, *17*, 20741–20753.

(58) Zheng, H.; Chen, B.; Yu, H.; Zhang, J.; Sun, J.; Li, X.; Sun, M.; Tian, B.; Fu, S.; Zhong, H. et al. Microwave-assisted hydrothermal synthesis and temperature sensing application of Er^{3+}/Yb^{3+} doped $NaY(WO_4)_2$ microstructures. *Journal of colloid and interface science* **2014**, *420*, 27–34.

List of Figures

TOC Graphic

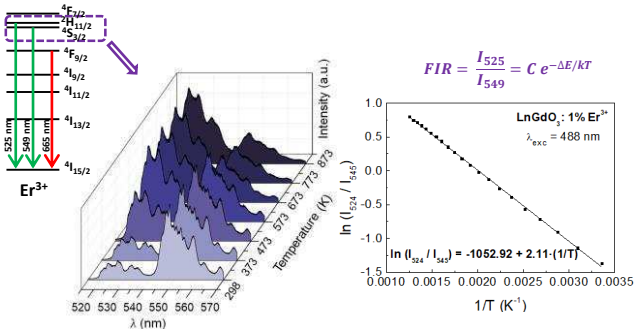
$^4F_{7/2}$
$^2H_{11/2}$
$^4S_{3/2}$
$^4F_{9/2}$
$^4I_{9/2}$
$^4I_{11/2}$
$^4I_{13/2}$
$^4I_{15/2}$
525 nm
549 nm
665 nm
Er^{3+}
Intensity (a.u.)
Temperature (K)
298
373
473
573
673
773
873
520 530 540 550 560 570
λ (nm)
$FIR = \frac{I_{525}}{I_{549}} = C\,e^{-\Delta E/kT}$
$LnGdO_3$: 1% Er^{3+}
λ_{exc} = 488 nm
ln (I_{524} / I_{545}) = -1052.92 + 2.11·(1/T)
ln (I_{524} / I_{545})
1.0
0.5
0.0
-0.5
-1.0
-1.5
0.0010 0.0015 0.0020 0.0025 0.0030 0.0035
1/T (K^{-1})

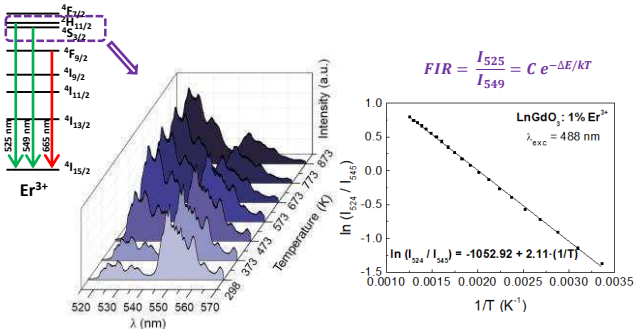
$^4F_{7/2}$
$^2H_{11/2}$
$^4S_{3/2}$
$^4F_{9/2}$
$^4I_{9/2}$
$^4I_{11/2}$
$^4I_{13/2}$
$^4I_{15/2}$
525 nm
549 nm
665 nm
Er^{3+}
Intensity (a.u.)
Temperature (K)
298
373
473
573
673
773
873
520 530 540 550 560 570
λ (nm)
$FIR = \frac{I_{525}}{I_{549}} = C\, e^{-\Delta E/kT}$
$LnGdO_3$: 1% Er^{3+}
λ_{exc} = 488 nm
ln (I_{524} / I_{545}) = -1052.92 + 2.11·(1/T)
ln (I_{524} / I_{545})
1.0
0.5
0.0
-0.5
-1.0
-1.5
0.0010 0.0015 0.0020 0.0025 0.0030 0.0035
1/T (K^{-1})